

# Computer simulation and experimental benchmarking of ultrashort pulse laser ablation of metallic targets

## Research Article

**Cite this article:** Suslova A, Elsied A, Hassanein A (2018). Computer simulation and experimental benchmarking of ultrashort pulse laser ablation of metallic targets. *Laser and Particle Beams* **36**, 144–153. <https://doi.org/10.1017/S0263034618000071>

Received: 20 December 2017  
Accepted: 15 February 2018

### Key words:

Explosive boiling; spallation; two-temperature model; ultrashort pulse laser ablation

### Author for correspondence:

A. Suslova, Center for Materials Under Extreme Environment (CMUXE), School of Nuclear Engineering, Purdue University, West Lafayette, IN 47907, USA, E-mail: [asuslova@purdue.edu](mailto:asuslova@purdue.edu), phone +1 765-409-6911

Anastassiya Suslova, Ahmed Elsied and Ahmed Hassanein

Center for Materials Under Extreme Environment (CMUXE), School of Nuclear Engineering, Purdue University, West Lafayette, IN 47907, USA

### Abstract

Integrated simulation results of femtosecond laser ablation of copper were compared with new experimental data. The numerical analysis was performed using our newly developed FEMTO-2D computer package based on the solution of the two-temperature model. Thermal dependence of target optical and thermodynamic processes was carefully considered. The experimental work was conducted with our 40 fs 800 nm Ti:sapphire laser in the energy range from 0.14 mJ to 0.77 mJ. Comparison of measured ablation profiles with simulation predictions based on phase explosion criterion has demonstrated that more than one ablation mechanisms contribute to the total material removal even in the laser intensity range where explosive boiling is dominating. Good correlation between experimental and simulation results was observed for skin depth and hot electron diffusion depth – two parameters commonly considered to identify two ablation regimes in metal. Analysis of the development dynamics for electron–lattice coupling and electron thermal conduction allowed explaining different ablation regimes because of the interplay of the two parameters.

## Introduction

Ultrashort pulse lasers (USPL) have numerous advantages over longer pulse laser when it comes to materials ablation for various applications. A distinctive feature of ultrashort pulse ablation is that laser–material interaction is separated in time from the actual removal of material. Therefore, the laser pulse energy is directly deposited into the solid target without self-shielding from the ablated plume typical for longer pulse lasers. Thus, ultrashort pulses provide a way of creating extremely higher energy densities in condensed matter with precise control over the ablated region. The combination of high power and extremely short pulse duration results in unique characteristics of the USPL–material interaction such as reduced heat affected zone (HAZ), ignition of ultrafast electron dynamics, and rapid formation and expansion of a strong plasma (Hypsh *et al.*, 2015).

However, the basic mechanisms leading to USPL induced ablation are poorly understood primarily due to extremely challenging experimental conditions, that is, time scales of the laser–matter interaction and complexity of physical processes needed to be considered for accurate computer simulation. Despite such difficulties, significant research efforts have been focused on developing a variety of simulation models with the aim of gaining a better understanding of the physical processes involved in the laser–matter interaction and their role in the different ablation mechanisms. Molecular-dynamics simulations (Perez & Lewis 2003; Hirayama & Obara 2005; Lewis & Perez 2009) and hydrodynamic modeling (Eidmann *et al.*, 2000; Colombier *et al.*, 2005) are often used to qualitatively describe USPL–solid target interaction. Different ablation mechanisms such as spallation, explosive boiling (phase explosion - PE), fragmentation, and vaporization have been identified and explored. Quantitative models applied to describe the experimental results are usually based on two-temperature model (TTM) (Anisimov *et al.*, 1974). Utilization of TTM allows to simulate the target thermodynamic evolution, which is not easily accessible through experiment. The knowledge of the thermodynamic evolution is a critical parameter to identify different USPL ablation regimes and mechanisms. In the present paper, we report experimental results on the interaction of femtosecond pulse laser with metal targets at laser intensities up to  $10^{14}$  W/cm<sup>2</sup>. In this laser intensity range, phase explosion (Miotello & Kelly 1995) is commonly considered as primary ablation mechanism for USPL with spallation potentially playing an important role (Zhigilei *et al.*, 2004, 2009; Lewis & Perez 2009). Numerical computations were carried out using our newly developed FEMTO-2D computer simulation code based on solving TTM (Suslova & Hassanein 2017a, b). We took great care to account for the strong temperature dependence of the material optical and thermodynamic properties under the condition of strong thermal non-equilibrium.

**Model description**

Theoretical analysis of femtosecond pulse laser interaction with metals applied in the FEMTO-2D simulation package is based on TTM model written for axially symmetric 2-D cylindrical coordinates (Suslova & Hassanein 2017b):

$$C_e \frac{\partial T_e}{\partial t} = \frac{1}{r} \frac{\partial}{\partial r} \left( k_e r \frac{\partial T_e}{\partial r} \right) + \frac{\partial}{\partial z} k_e \frac{\partial T_e}{\partial z} - G(T_e - T_l) + S(r, z, t) \tag{1}$$

$$C_l \frac{\partial T_l}{\partial t} = \frac{1}{r} \frac{\partial}{\partial r} \left( k_l r \frac{\partial T_l}{\partial r} \right) + \frac{\partial}{\partial z} k_e \frac{\partial T_e}{\partial z} + G(T_e - T_l) \tag{2}$$

where  $r$  is the radial distance from the center of the beam and  $z$  is the coordinate normal to the sample surface with the origin at the surface.

The main laser absorption mechanism in metals is inverse bremsstrahlung absorption by free electrons (Zhao 2014) followed by the rapid increase in electron temperature while lattice remains relatively cold, and the target density is unchanged during the laser pulse (Gamaly 2011). The laser heat source component within the film layer was modeled using Gaussian temporal and spatial (radial) profiles, and an exponential attenuation of the laser intensity with depth according to the Beer–Lambert law (Suslova & Hassanein 2017b):

$$S(z, r, t) = \sqrt{\frac{\beta(1-R)}{\pi t_p \alpha_{opt}}} I_0 \exp\left[-\left(\frac{z}{\alpha_{opt}}\right)\right] \exp\left[-\frac{r^2}{2\sigma^2}\right] \exp\left[-\beta^* \left(\frac{t-2t_p}{t_p}\right)^2\right] \tag{3}$$

where,  $I_0$  is the laser pulse peak intensity,  $R$  is the temperature dependent reflectivity,  $\alpha_{opt}$  is the temperature dependent optical penetration depth,  $t_p$  is the laser pulse full width at half-maximum,  $\sigma$  is profile parameter, and parameter  $\beta = 4 \ln(2)$ .

Optical and thermophysical properties of target materials were defined as temperature dependent parameters; a detailed description of the analytical models was provided in Suslova and Hassanein (2017a, b). For electron subsystem, *electron heat capacity* ( $C_e$ ) and *thermal conductivity* ( $k_e$ ) were defined via smooth interpolation between two polar states of the material, that is, the cold solid state and hot dense plasma state as following:

$$C_e = n_e k_B \frac{3\pi^2 T_e}{\sqrt{36T_F^2 + 4\pi^4 T_e^2}} \tag{4}$$

$$k_e = \sqrt{\left(\frac{C_e v_F^2}{3v_{eff}}\right)^2 + \left(\frac{128(0.24 + Z)n_e T_e}{3\pi(4.2 + Z)m_e(v_{e-i} + v_{e-e})}\right)^2} \tag{5}$$

where  $v_{e-i}$ ,  $v_{e-e}$  are electron–ion and electron–electron collision frequencies,  $n_e = Zn_i$  is electron density,  $Z$  is the average charge state at given  $T_e$ ,  $n_i$  is the ion density,  $T_F$  is Fermi temperature,  $v_F$  is Fermi velocity, and  $k_B$  is Boltzmann constant. Details of the applied collision theory and its role in the calculation of electron and lattice thermodynamic properties, and material optical properties were given in (Suslova & Hassanein 2017b).

The lattice heat capacity was considered as constant ( $C_l(\text{Cu}) = 3.5 \text{ J/cm}^3\text{K}$ ) because of its weak dependence on the lattice temperature.

The lattice heat conductivity was approximated based on the collisional theory as follows:

$$k_l = \frac{1}{3} C_l \frac{\vartheta_i^2}{v_{i-i}} \tag{6}$$

where

$$\vartheta_i = \sqrt{\frac{2k_B T_i}{m_i} + C_s^2}$$

is the ion/phonon velocity at given lattice temperature, and  $v_{i-i} = n_i \pi (2r_0)^2 \vartheta_i$  is the ion–ion collisional frequency calculated based on hard sphere model,  $m_i$  is atomic mass, and  $r_0$  is the atomic radius.

The temperature dependent *electron–phonon coupling factor* was adopted from recent theoretical model (Lin 2007; Lin et al., 2008) that takes into account the electron density of states in the material, since it has been shown that electron–phonon coupling factor is very sensitive to details of the electronic structure of the material. For the electron temperature range above 4.3 eV, the model was further extended to higher electron temperature range with the formula for electron–ion coupling in plasma:

$$G = 3 \frac{m_e}{m_i} v_{e-i} Z n_i k_B.$$

The following initial and boundary conditions were applied to solve Eqns. (1) and (2). The simulation started at time  $t = 0$ . The initial temperature for electrons and lattice, as well as the temperatures far away from the exposed surface in the  $z$ -direction and far from the center in  $r$ -direction at any time step, are set at the ambient temperature (300 K). Thermal emission from the surface of the target during simulation was accounted for with the Stefan–Boltzmann law. For the other outer boundaries, zero heat losses to the surrounding vacuum were assumed during the entire calculation time:

$$\left. \frac{dT_e}{dr} \right|_0 = \left. \frac{dT_l}{dr} \right|_0 = \left. \frac{dT_e}{dz} \right|_r = \left. \frac{dT_l}{dz} \right|_r = 0,$$

and

$$\left. \frac{dT_e}{dz} \right|_z = \left. \frac{dT_l}{dz} \right|_z.$$

Phase transformations from solid to liquid and from liquid to solid were treated as isothermal phase changes. The lattice temperature remained constant ( $T_l = T_{\text{melt}}$ ) during the phase change process until the transformation is completed. The phase transformation was considered completed when the net heat absorbed (for melting) or released (for solidification) within the control volume became equal to the fusion latent heat:

$$\rho_l H_m = \int_{t_{\text{chst}}}^{t_{\text{chfn}}} \left[ \frac{1}{r} \frac{\partial}{\partial r} \left( k_l r \frac{\partial T_l}{\partial r} \right) + \frac{\partial}{\partial z} k_l \frac{\partial T_l}{\partial z} + G(T_e - T_l) \right] dt \tag{7}$$

where  $t_{\text{chst}}$  is a time when phase transformation begins and  $t_{\text{chfn}}$  is a time when phase transformation fully completed. Once melting begins, the two phases exist simultaneously separated by a moving interface. The location of the solid–liquid interface was tracked, and interphase velocity was calculated based on the energy balance equation at the interface (Hassanein 1983):

$$\left[ 1 + \left( \frac{\partial z_m}{\partial r} \right)^2 \right] \left[ k_1^s \frac{\partial T_1^s}{\partial z} - k_1^l \frac{\partial T_1^l}{\partial z} \right] = \rho_l H_m u_{sl} \quad (8)$$

where  $z_m$  is the location of the interface,  $u_{sl}$  is the interface velocity, upper case s denotes a solid state and upper-case l stays for a liquid phase.

The location of the liquid phase–solid interface has been tracked through the simulation time to estimate the melted zone, assuming no material removal may originate from outside of the melted pool.

Two material removal mechanisms were considered for the model. Material removal via normal evaporation was estimated by considering receding surface at the interphase between vapor and solid or liquid. The velocity of the receding interface is a highly non-linear function of temperature and calculated with following equation (Hassanein *et al.*, 1984):

$$\mathfrak{D}_{\text{surface}}(r, t) = 0.058 \frac{\sqrt{A} P_V(T_V)}{\rho_V(T_V) \sqrt{T_V}} \quad (9)$$

$$P_V = P_0 \exp\left(-\frac{H_V}{k_B T_V}\right) \quad (10)$$

where  $A$  is atomic mass number,  $P_V$  is vapor pressure as a function of vapor temperature, and latent heat of vaporization  $H_V$ ,  $T_V$  is target temperature at the surface,  $\rho_V$  target density at given temperature, and  $P_0$  is the reference pressure.

The second ablation mechanism considered is explosive boiling (phase explosion). Phase explosion takes place when the material is superheated to the thermodynamic equilibrium critical temperature point  $T_{\text{cr}}$  due to rapid laser energy absorption by electrons and following heat transfer to the lattice on the time scale shorter than the time required for a normal boiling to occur (Sokolowski-Tinten *et al.*, 1998; Bulgakova & Bourakov 2002; Lewis & Perez 2009). The typical time span for the normal boiling is in the range of 100 ps (Yang *et al.*, 2007). For the phase explosion, we considered the commonly applied (Chicbkov *et al.*, 1996; Chen & Beraun 2003; Yang *et al.*, 2007; Li *et al.*, 2011; Wang *et al.*, 2013) condition for the lattice temperature reaching  $0.9 T_{\text{cr}}$ .

## Experimental details

The experimental work was conducted at the Center for Materials Under eXtreme Environment (CMUXE) in the High Energy Density Physics laboratory (HEDP Lab) with chirped pulse amplified Ti:Sapphire femtosecond laser system operating at 800 nm wavelength. The contrast of the laser system is  $\sim 10^{-7}$ . The following laser system parameters were used during the experiment: minimum pulse duration – 40 fs, repetition rate – 1 Hz, beam diameter on the target – 100  $\mu\text{m}$ , the laser pulse energy range – from 140  $\mu\text{J}$  to 770  $\mu\text{J}$  (corresponds to laser intensity ranges from  $2 \times 10^{13}$  W/cm<sup>2</sup>

to  $1.1 \times 10^{14}$  W/cm<sup>2</sup>). All experiments were conducted at normal incidence at the base pressure of  $\sim 10^{-5}$  Torr.

Targets were made of commercially available copper samples mechanically polished to a mirror-like surface. Due to slow ablation rate at low laser fluence, the experiments were performed with 20 laser shots, and the ablation rate was then defined as the maximum crater depth per laser shot. The accumulation of the residual heat was assumed to have a negligible effect because of the extremely short pulse duration compared with the cooling time between pulses.

After irradiation, samples were imaged with scanning electron microscope (SEM); ablation profiles were characterized with optical microscope profilometer and with cross-sectional SEM images obtained with FIB SEM. For the optical profilometer, lateral resolution was  $\sim 2 \mu\text{m}$  and depth resolution was  $\sim 1$  nm.

## Results and discussion

### Analysis and comparison of FEMTO-2D simulation with the experimental data

The aim of this work was to test our developed simulation package for USPL–matter interaction to predict laser-induced ablation and to gain a better understanding of the material removal processes through careful analysis of experimental data and simulated results. Copper was chosen as target material for being affordable, available, and extensively studied.

First, we have determined target melting threshold in given experimental setup, since no material removal is possible before enough energy has been supplied to the target and melting occurs. FEMTO-2D simulation predicted the melting threshold for copper at laser fluence around 0.6 J/cm<sup>2</sup> which corresponds to about 0.045 J/cm<sup>2</sup> of absorbed energy density.

The absorption efficiency is one of the parameters that should be carefully analyzed when investigating the interaction of the USPLs with condensed matter. Many analytical models and experimental work (Preuss *et al.*, 1995; Price *et al.*, 1995; Fisher *et al.*, 2001, 2005; Kirkwood *et al.*, 2009; Loboda *et al.*, 2011) have demonstrated that the material optical properties are defined by the collisional processes inside the material. The absorption efficiency as a function of laser fluence in copper was calculated based on FEMTO-2D simulations and compared with available experimental data in Suslova and Hassanein (2017b). Figure 1 shows how the absorption efficiency of copper changes as a function of the incident laser pulse fluence in the range considered for this work compared with the fixed value determined at room temperature.

As seen from Figure 1, absorption efficiency for copper target increases by an order of magnitude within the laser fluence range considered in our work. Therefore, to account for changes in optical properties and its effect on the ablation, we consider absorbed laser fluence for further analysis.

Next, an ablation threshold fluence of 0.27 J/cm<sup>2</sup> was defined for explosive boiling based on our simulations as the fluence at which the maximum lattice temperature at the surface reaches the temperature criterion for phase explosion ( $0.9 T_{\text{cr}}$ ). Based on this parameter, we concluded that all except one of our experimental data correspond to the ablation regime with explosive boiling.

FEMTO-2D simulation predictions of the ablation and melted zone profiles were compared with ablation profiles from experiment measured using optical microscope profilometer for four

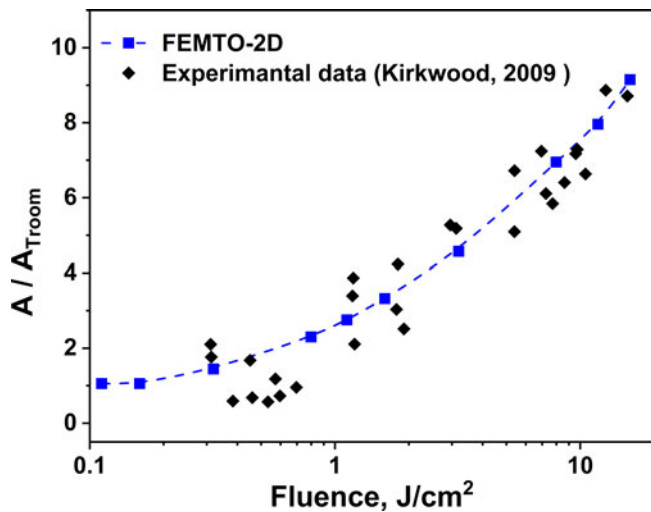


**Fig. 1.** Copper absorption normalized to the constant value at room temperature as function of the laser fluence. Comparison of FEMTO-2D simulations to experimental data by Kirkwood *et al.* (2009).

laser energies: 0.14 mJ (corresponds to 0.2 J/cm<sup>2</sup> absorbed fluence), 0.2 mJ (corresponds to 0.28 J/cm<sup>2</sup> absorbed fluence), 0.4 mJ (corresponds to 0.91 J/cm<sup>2</sup> absorbed fluence), and 0.77 mJ (corresponds to 2.37 J/cm<sup>2</sup> absorbed fluence) as shown in Figure 2. At lowest laser fluence, FEMTO-2D predicts extremely shallow ablation profile solely due to evaporation; therefore, the additional scale was used for simulated ablation depth for 0.14 mJ laser pulse.

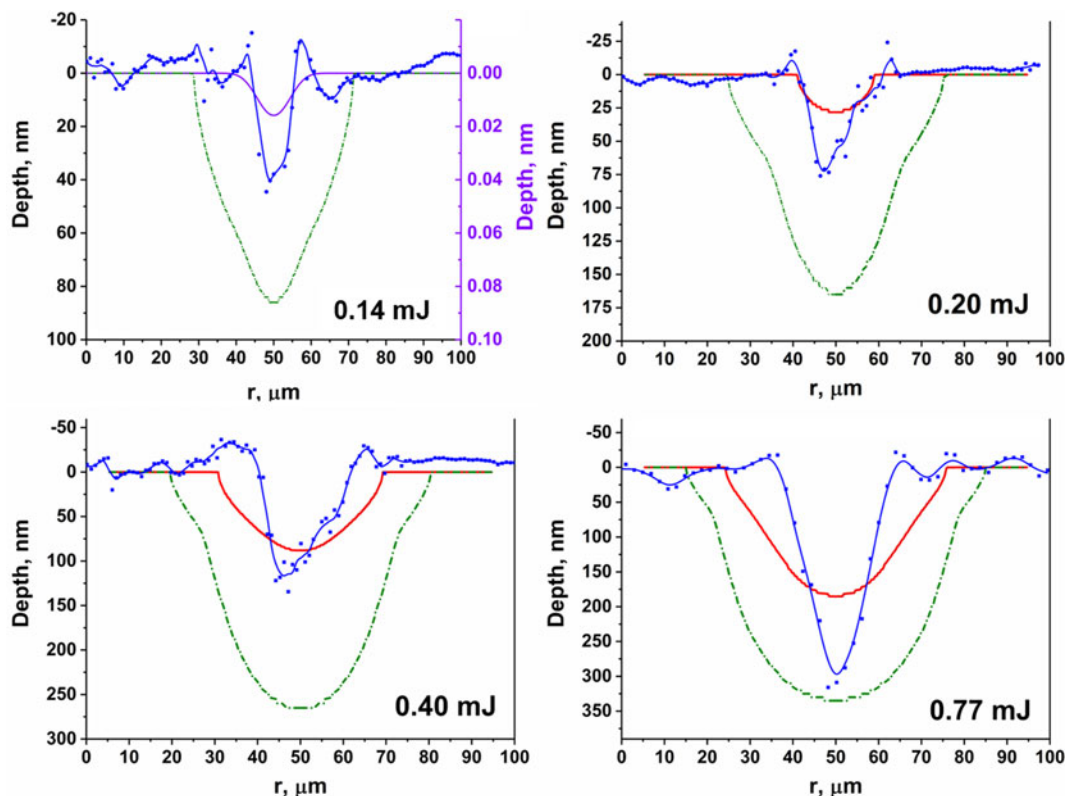


**Fig. 2.** Comparison of simulated melted zone profiles (dash-dotted green line), ablation via evaporation (purple line) for (a) 0.2 J/cm<sup>2</sup>, and ablation via pure phase explosion (red solid line) profiles for (b) 0.28 J/cm<sup>2</sup>, (c) 0.91 J/cm<sup>2</sup>, and (d) 2.37 J/cm<sup>2</sup> with experimental data by optical profilometer (blue dots).

Analysis of the FIB cross-sectional SEM image of ablation profiles for 0.2 J/cm<sup>2</sup> and 0.28 J/cm<sup>2</sup> laser pulses (Fig. 3) confirms the measured maximum depth of the ablated crater. It also reveals the effect of the poor lateral resolution of the optical profilometer. Cross-sectional SEM images show very localized damage induced by USPLs with no cracks observed at the samples' surfaces and underneath.

In Figure 4, FEMTO-2D simulation predictions of ablation rate and melted pool depth for a single pulse as a function of absorbed laser fluence were compared with the experimental results predicted based on optical profilometry measurements. For convenience, logarithmic and semi-logarithmic scales were used.

The first observation from Figures 2 and 4 is that our simulation predictions tend to underestimate the ablation rate in the given range of laser fluences. As described, FEMTO-2D accounts for two material removal mechanisms: evaporation and phase explosion, with the later proven to be dominant at the fluences above the phase explosion ablation threshold (simulated absorbed fluence of 0.27 J/cm<sup>2</sup>). However, in reality, several different material removal mechanisms identified for USPL induced ablation contribute to the final ablation rate (Price *et al.*, 1995; Perez & Lewis 2002). Several MD simulations (Perez & Lewis 2003; Lewis & Perez 2009; Zhigilei *et al.*, 2009) demonstrated that at laser fluence just above the damage (melting) threshold, spallation is a dominating ablation mechanism. The spallation regime requires satisfaction of the requirement of stress confinement (for pulses below 1 ps pulse duration), and it is identified by significant melting and material removal in the form of large droplets. The transition from spallation to explosive boiling happens at

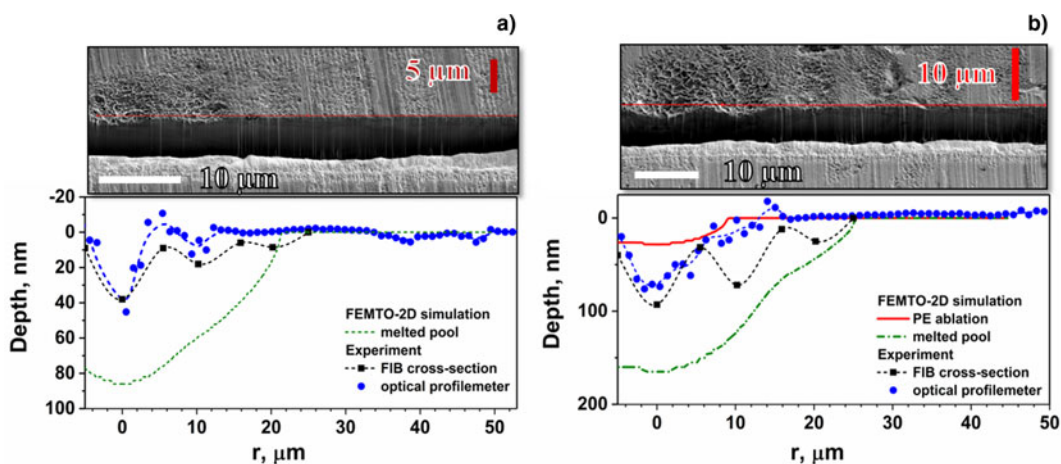


Fig. 3. Comparison of experimentally measured profiles (FIB-SEM and profilometer) with simulated predictions for (a) 0.20 J/cm<sup>2</sup> and (b) 0.28 J/cm<sup>2</sup> laser pulses.

higher laser intensities, and phase explosion becomes dominant. In FEMTO-2D simulations, phase explosion is considered as ‘pure’ explosive boiling solely based on the thermal criterion since TTM does not provide a way to account for the stress confinement induced by the USPLs. It was pointed out that phase explosion occurring under conditions of stress confinement takes place simultaneously with the relaxation of the laser-induced stresses, resulting in a more vigorous material ejection and higher ablation yields as compared to a “pure” phase explosion (Zhigilei *et al.*, 2009). Therefore, it was expected to have lower ablation rate based on the simulations compared with experimental results. Based on the observation that the material removal depth in experiment never went beyond the simulated depth for a liquid phase at any considered laser intensity, FEMTO-2D proved to be useful for simulation and analysis of USPL induced ablation.

The second observation is that like many reported experimental results for USPL induced ablation, our experimental data clearly show two ablation regimes (Preuss *et al.*, 1995; Furusawa *et al.*, 1999; Hashida *et al.*, 2002; Colombier *et al.*, 2005; Hirayama & Obara 2005; Wang *et al.*, 2013). In literature, the first ablation regime at lower laser fluence is usually associated with the skin depth. It is assumed that due to low free electron density the energy transfer occurs only within the area

characterized by the skin depth (an effective absorption depth)  $d$  (Furusawa *et al.*, 1999). The ablation rate can then be fitted with the following logarithmic function:  $L = d \ln(F/F_{th}^{skin})$ . Fitting our experimental data into the equation predicts  $d = 50$  nm and  $F_{th}^{skin} \approx 2F_{melt} = 0.09$  J/cm<sup>2</sup>. For metallic targets, the skin depth is often referred as combination of the optical penetration depth and ballistic electron range, and it represents the depth of laser energy deposition inside the target (Wellershoff *et al.*, 1999; Hohlfeld *et al.*, 2000; Schmidt *et al.*, 2002). The capability of FEMTO-2D simulation package to account for ballistic heat transfer and to predict the heat flux penetration profile was discussed in Suslova and Hassanein (2018). An effective absorption depth was defined right after the laser pulse as the depth where maximum electron temperature (offset by 300 K) drops by a factor of  $e$ . The effect of ballistic electrons on the heat flux deposition profile is significant at low laser fluences and reduces considerably as the laser fluence increases due to higher electron density (Furusawa *et al.*, 1999). Recent experimental work (Chen *et al.*, 2012) and our recent simulation results (Suslova & Hassanein, 2018) demonstrated that the ballistic component of the heat transfer becomes negligible above particular laser fluence. Based on the FEMTO-2D simulations for copper presented in Figure 5, the role of the ballistic heat transport in the initial heat distribution inside the target diminishes for the absorbed fluence range from

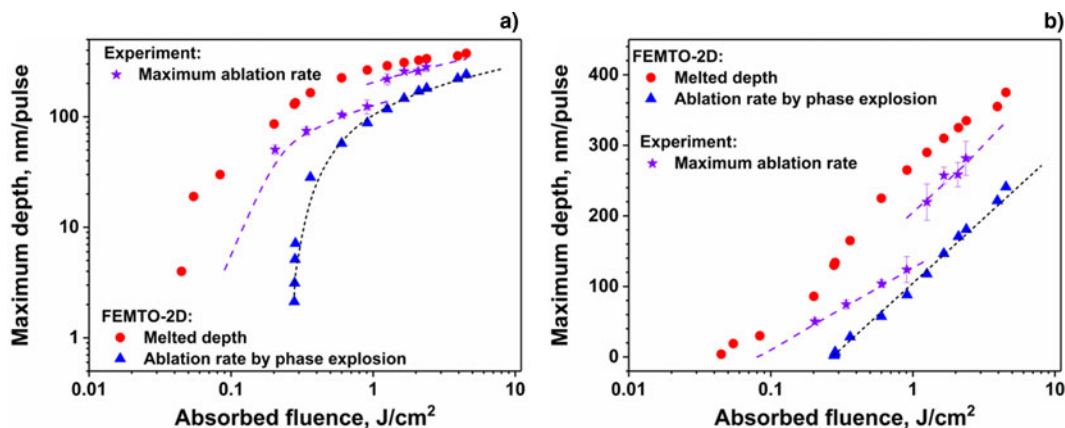


Fig. 4. Comparison of experimental ablation rate to simulated ablation rate and melted pool depth: (a) – logarithmic scale, (b) – semi-logarithmic scale.

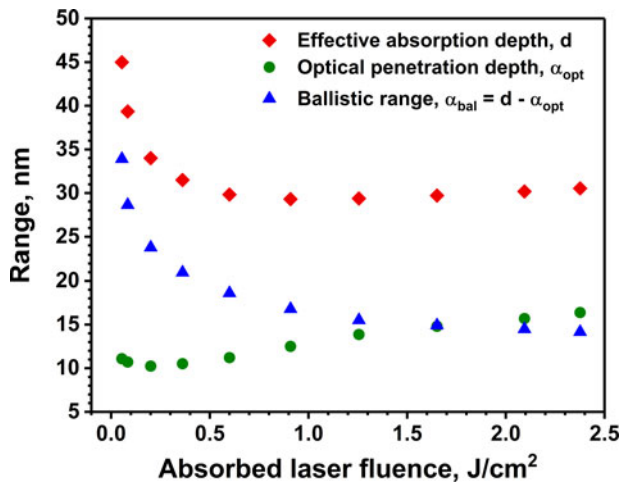


Fig. 5. FEMTO-2D simulation of the effective absorption depth of the laser pulse in copper.

melting threshold to around  $0.9 \text{ J/cm}^2$ . The latter marks the upper limit for ballistic heat transport effect and corresponds to the end of the first ablation regime observed experimentally. Figure 5 shows how the effective laser absorption depth is determined right after the laser pulse, simulated temperature dependent optical penetration depth, and calculated ballistic range change with laser fluence in the low range of the fluences considered in this work.

The maximum effective absorption depth for the laser intensity range between melting threshold and the end of the first ablation regime is 45 nm which close to the theoretically calculated electron mean-free path in copper at room temperature (42 nm) (Byskov-Nielsen *et al.*, 2011), optical penetration depth ( $42.7 \pm 0.85 \text{ nm}$ ) determined based on the experimental results in Mannion *et al.* (2004), and to the fitted value for  $d$  based on our experimental data. At laser fluences above  $0.9 \text{ J/cm}^2$ , the estimated ballistic range remains at an almost constant value of 15 nm. This value for the ballistic range is commonly used to account for ballistic electron heat transport in copper (Byskov-Nielsen *et al.*, 2011; Cheng & Chen 2016). Thus, although FEMTO-2D is not designed to quantitatively predict the ablation profile due to the complexity of different ablation mechanisms, it confirms that the first ablation regime is related to the depth of the initial heat deposition when ballistic heat transport dominates over diffusive transport.

The second ablation regime is commonly referred to the case when hot electrons penetrate significantly deeper than skin layer before transferring their energy to the lattice. In literature, the second ablation regime is usually fitted with a function similar to the low fluence regime logarithmic function:  $L = l \ln(F/F_{th}^{td})$ , where  $l$  corresponds to the electron thermal diffusion length. For copper,  $l$  found to be equal 80 nm at the threshold fluence of  $1 \text{ J/cm}^2$  (Hashida *et al.*, 2002). In the fluence range from  $1.26 \text{ J/cm}^2$  to  $2.36 \text{ J/cm}^2$ , the fitting function is in a good correlation with our experimental results (Fig. 2).

In addition, FEMTO-2D simulation results of ablation rate due to the phase explosion for the considered range of the laser intensities can also be fitted with logarithmic function  $L = l \ln(F/F_{th}^{pe})$ , where  $l$  is the fitting parameter representing thermal conduction depth, and  $F_{th}^{pe}$  is simulated threshold for explosive boiling. The best fit was achieved with  $l$  equal 80 nm. This was expected

since phase explosion is purely temperature controlled ablation mechanism defined by the heat propagation dynamics.

#### Analysis of material ablation dynamics for two ablation mechanisms: spallation and explosive boiling

Despite FEMTO-2D ability to match the experimental results, the logarithmic fitting model discussed above does not provide detail information on the physical mechanisms of the material removal. Moreover, the fitting parameters are often determined based on the experimental data without clear theoretical explanation. To gain more understanding of the material removal dynamics, we have analyzed SEM images of four laser shots in our experiment considering MD simulation results presented in (Zhigilei *et al.*, 2009) and our FEMTO-2D predictions (Fig. 6).

FEMTO-2D simulations predict no material removal via phase explosion at laser fluences below  $0.27 \text{ J/cm}^2$ . The transition from spallation to explosive boiling can be characterized by the change in the composition of the ejected ablated plume, that is, from large liquid droplets to a mixture of the small droplets and vapor-phase atoms (Zhigilei *et al.*, 2009). Comparing two SEM images of the center spots of the laser shots at  $0.20 \text{ J/cm}^2$  (0.14 mJ) and  $0.28 \text{ J/cm}^2$  (0.20 mJ), we observed very few 'loose' particles at the lowest laser energy below the phase explosion threshold. However, at laser fluence right above the threshold ( $F_{th} = 0.27 \text{ J/cm}^2$ ), the particles density increases more than twice (Fig. 7) with the particles minimum size decreasing more than twice (Fig. 8) from around 80 nm to around 30 nm (based on the analysis of three different laser spots for each fluence). We attribute the drop in the minimum particle size to initiation of ablation via phase explosion. Further analysis showed that the minimum particles size at all fluences above the threshold for explosive boiling remained nearly the same. The analysis of the particle size distribution (Fig. 9) also shows an increasing fraction of the smaller particles at higher laser fluences. The observed particles density in the central region is linearly increasing as a function of the laser fluence up to  $1 \text{ J/cm}^2$ . At the higher laser intensity, the role of the explosive boiling in the total ablation is increasing significantly and becomes dominant; therefore, the smaller fraction of the ablated material is redeposited in the central region in form of droplets or small particles. Extrapolating the linear trend to the lower laser fluence gives an ablation threshold fluence in our experiment which is the same value for the spallation ablation threshold as estimated from the logarithmic fitting function  $F_{th}^{skin} \approx 2F_{melt} = 0.09 \text{ J/cm}^2$ .

#### The role of electron heat conduction and electron-lattice heat transfer dynamics at different ablation regimes

Another aspect of laser-material interactions, considered in this work is the interplay between electron-lattice coupling and hot electron heat transport during thermalization time. These two simultaneous processes are main factors that determine the material ablation rate and specific removal depth. The specific removal depth in this work is defined as the depth removed per unit incident fluence. Figure 10a shows how specific removal depth changes as a function of the laser fluence. We have identified three regions: first region characterized by extremely small specific removal depth due to evaporation; the second region coincides with the first ablation regime; and the third region coincides with the second ablation regime. The second region is characterized by rapidly increasing specific removal depth which reaches the maximum at around  $1 \text{ J/cm}^2$ . In the third region, the specific

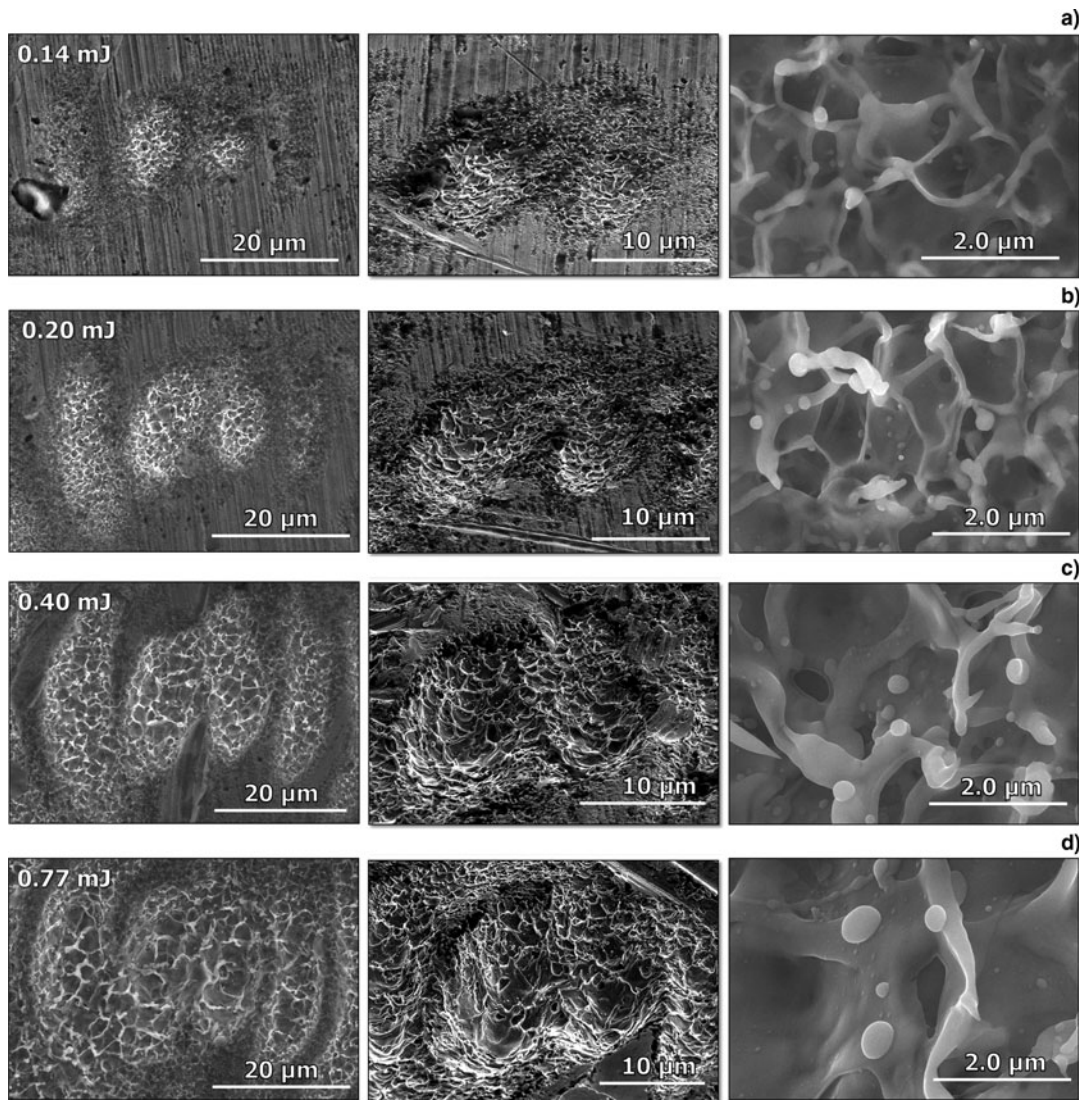


**Fig. 6.** SEM images of the central spot of the laser for (a)  $-0.20 \text{ J/cm}^2$ , (b)  $-0.28 \text{ J/cm}^2$ , (c)  $-0.91 \text{ J/cm}^2$ , (d)  $-2.37 \text{ J/cm}^2$ . Central column images were taken at  $52^\circ$  sample stage tilt.

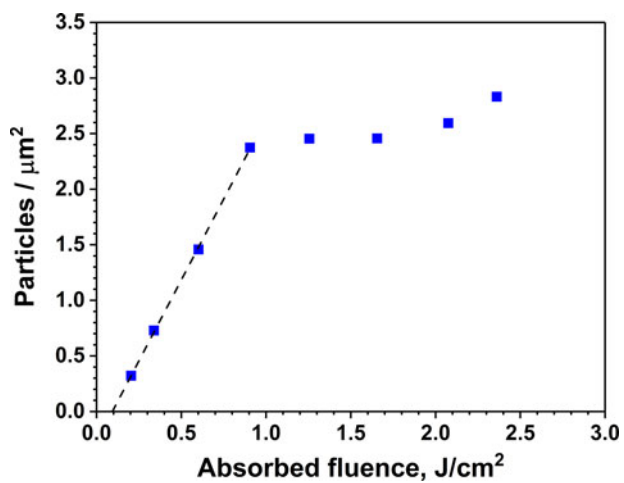


**Fig. 7.** Average particles density versus laser fluence.

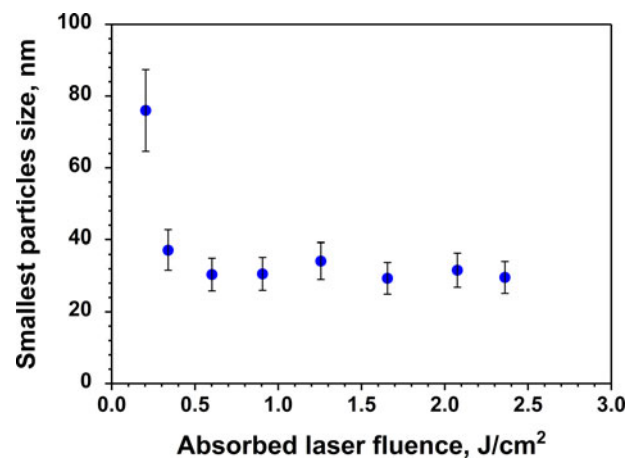


**Fig. 8.** Size of the smallest particles at different laser fluences.

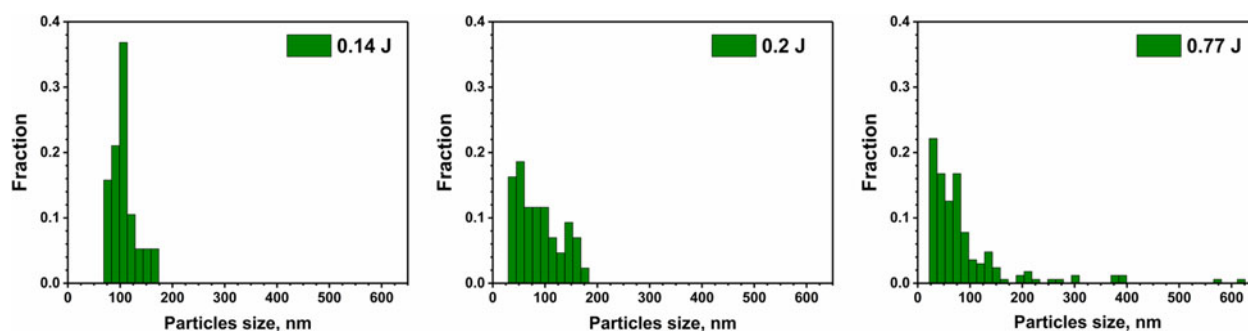


Fig. 9. Normalized particles size distribution.

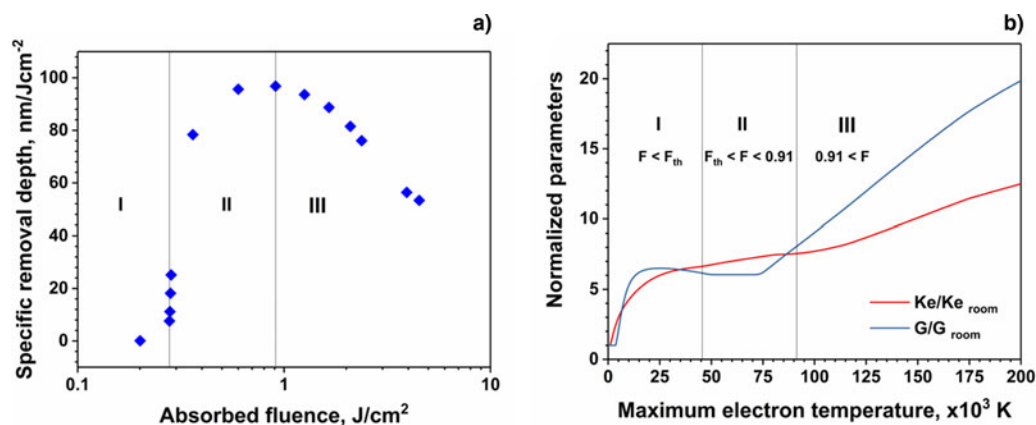


Fig. 10. (a) Specific removal depth versus laser fluence; (b) Temperature dependence of coupling factor and electron thermal conductivity normalized to corresponding room temperature values.

removal depth starts decreasing, indicating reduced laser ablation efficiency. Similar trends were observed in several experimental works (Colombier *et al.*, 2005; Polek 2015).

Next, we have compared the behavior of the coupling factor and the hot electron conductivity (considering also a contribution from ballistic electrons) as a function of the electron temperature. To directly compare these two parameters, we have normalized them to their room temperature values. Three regions discussed in Figure 10a were identified on the Figure 10b with respect to the maximum electron temperature at given laser fluence. Based on the scope of this work, we focused on the regions II and III. As one can see from Figure 10b, region II corresponds to the electron temperature diapason where electron thermal conductivity has increased slightly more than coupling factor compared with their room temperature values. This means hot electrons can travel deeper into the target before depositing their energy to the lattice. As the electron temperature decreases, the coupling of electron energy to lattice is still taking place but at a slower rate. However, this region also coincides with the range where ballistic electrons play a significant role in the heat transfer and define the ablation profile. The third region is characterized by significantly faster-increasing coupling factor compared with the increase in thermal conductivity. Therefore, due to decreasing thermalization time, the distance that hot electrons can travel before reaching thermal equilibrium with lattice is increasing slower than in the second region. It is not very clear if such coincidence of regions for different specific removal depth trends, the transition between two discussed ablation mechanisms, and two

ablation regimes indicate a direct connection to the material thermodynamic properties. More careful experimental and analytical analysis is required for different target materials to draw a conclusion.

## Conclusion

Simulation results of femtosecond laser ablation of copper were compared with new experimental data. The numerical analysis was performed using our newly developed FEMTO-2D computer package based on the solution of the two-temperature model. Based on the analysis of the experimental results, we conclude that more than one ablation mechanism is contributing to the total material removal at the considered laser intensities in this study. Even though explosive boiling is commonly considered as dominant ablation mechanism for the USPL induced ablation, the 'pure' phase explosion simulated based on the temperature profiles underestimates the total material removal. We attributed that to the expected enhancement of the explosive boiling ablation under the condition of the stress confinement satisfied for sub-picosecond laser pulses. With FEMTO-2D simulation package, based on the solution of the two-temperature model, we could estimate the maximum possible ablation depth by simulating the melted pool profile. However, predicted ablation profile based on the phase explosion criterion slightly underestimates material removal rate at the investigated laser intensities. Another factor that might have also contributed to the difference in ablation profiles between experiment and computer simulation

is due to multiple shots used during experiment versus single shot predictions from simulations. Multiple shots were used in our experiment because of very low ablation rate at the given laser fluences such that ablation from the single shot near threshold fluence would be comparable, for example, to the surface morphology resulted from polishing. Further investigation on the effect of a number of pulses on ablation depth at different laser fluence is required to evaluate the significance of this factor. Nevertheless, FEMTO-2D simulations provided additional details to enhance our understanding of the ablation mechanisms in metals during femtosecond laser interactions with materials.

We found that during the fast ablation regime, that is, when the ablation rate increases significantly with the laser intensity at low laser fluence, can be correlated with the intensity range where ballistic electrons play a dominant role in heat transfer. Simulated laser intensity limit for ballistic electrons domination corresponds to the upper limit of the first ablation regime where material removal depth is associated with the skin layer depth. The predicted maximum effective laser deposition range (can be interpreted as skin layer depth) is similar to the fitting parameter for the first ablation regime based on our experimental data. We also observed a rapid growth of specific removal depth with increasing absorbed laser fluence for laser intensity range corresponding to the fast ablation regime. After the transition to the second ablation regime, specific removal depth starts to decrease with increasing absorbed laser fluence. We have demonstrated that by analyzing the relation between electron thermal conductivity and electron–lattice coupling factor calculated using FEMTO-2D, it is possible to predict the transition zone between two ablation regimes. This allows predicting laser parameters corresponding to the maximum efficiency of laser-induced ablation (depth removed per energy unit). Our experimental results demonstrate that two ablation mechanisms (spallation and phase explosion) may simultaneously contribute to the total material ablation in the first ablation regime with a significant increase of phase explosion role with laser intensity.

For the second ablation regime, experimental data for different laser intensities follows the same trend as simulated ablation rate for explosive boiling and they both can be fitted with the well-known logarithmic function. The explanation is that the second ablation regime is associated with the hot electron diffusion depth, which is directly defined by the electron temperature. The phase explosion – a purely temperature controlled ablation mechanism, is defined by heat propagation dynamics. The simulation data show that laser ablation efficiency for the second ablation regime is lower than the first ablation regime. We attributed that to faster increasing coupling factor compared with the electron thermal conductivity. High coupling factor results in a rapid heating, which is the main reason for the phase explosion. Analysis of SEM images from our experiments also supports the hypothesis that phase explosion is a dominant ablation mechanism for the second ablation regime.

**Acknowledgments.** This work is partially supported by the NSF, PIRE project.

## References

Anisimov SI, Kapeliovich BL and Perelman TL (1974) Electron emission from metal surfaces exposed to ultrashort laser pulses. *Journal of Experimental and Theoretical Physics* **66**, 776–781.

- Bulgakova NM and Bourakov IM (2002) Phase explosion under ultrashort pulsed laser ablation: modeling with analysis of metastable state of melt. *Applied Surface Science* **197–198**, 41–44.
- Byuskov-Nielsen J, Savolainen J-M, Christensen MS and Balling P (2011) Ultra-short pulse laser ablation of copper, silver and tungsten: experimental data and two-temperature model simulations. *Applied Physics A* **103**(2), 447–453.
- Chen JK and Beraun JE (2003) Modelling of ultrashort laser ablation of gold films in vacuum. *Journal of Optics A: Pure and Applied Optics* **5**(3), 168–173.
- Chen Z, Sametoglu V, Tsui YY, Ao T and Ng A (2012) Flux-Limited Nonequilibrium Electron Energy Transport in Warm Dense Gold. *Physical Review Letters* **108**(16), 165001.
- Cheng C-W and Chen J-K (2016) Drilling of Copper Using a Dual-Pulse Femtosecond Laser. *Technologies* **4**(1), 7.
- Chibikov BN, Momma C, Nolte S, Von Alvensleben F and Tiinnermann A (1996) Femtosecond, picosecond and nanosecond laser ablation of solids. *Applied Physics* **63**, 109–115.
- Colombier JP, Combis P, Bonneau F, Le Harzic R and Audouard E (2005) Hydrodynamic simulations of metal ablation by femtosecond laser irradiation. *Physical Review B* **71**(16), 165406.
- Eidmann K, Meyer-ter-Vehn J, Schlegel T and Hüller S (2000) Hydrodynamic simulation of subpicosecond laser interaction with solid-density matter. *Physical Review E* **62**(1), 1202–1214.
- Fisher D, Fraenkel M, Henis Z, Moshe E and Eliezer S (2001) Interband and intraband (Drude) contributions to femtosecond laser absorption in aluminum. *Physical Review E* **65**(1), 16409.
- Fisher D, Fraenkel M, Zinamon Z, Henis Z, Moshe E, Horovitz Y, Luzon E, Maman S and Eliezer S (2005) Intraband and interband absorption of femtosecond laser pulses in copper. *Laser and Particle Beams* **23**(3), 391–393.
- Furusawa K, Takahashi K, Kumagai H, Midorikawa K and Obara M (1999) Ablation characteristics of Au, Ag, and Cu metals using a femtosecond Ti:sapphire laser. *Applied Physics A: Materials Science & Processing* **69**(7), S359–S366.
- Gamaly E (2011) *Femtosecond Laser-Matter Interaction: Theory, Experiments and Applications*. Singapore: Pan Stanford Publishing Pte. Ltd.
- Hashida M, Semerok A, Gobert O, Petite G, Izawa Y and Wagner J - (2002) Ablation threshold dependence on pulse duration for copper. *Applied Surface Science* **197–198**, 862–867.
- Hassanein A (1983) *Modeling the interaction of high power ion or electron beams with solid target materials*. Report No. ANL/EPP/TM-179. Chicago, IL: Argon National Laboratory.
- Hassanein A, Kulcinski GL and Wolfer WG (1984) Surface melting and evaporation during disruptions in magnetic fusion reactors. *Nuclear Engineering and Design. Fusion* **1**(3), 307–324.
- Hirayama Y and Obara M (2005) Heat-affected zone and ablation rate of copper ablated with femtosecond laser. *Journal of Applied Physics* **97**(6), 64903.
- Hohlfeld J, Wellershoff S-S, GÜdde J, Conrad U, Jähnke V and Matthias E (2000) Electron and lattice dynamics following optical excitation of metals. *Chemical Physics* **251**(1), 237–258.
- Hyphs S, Shannon J and Shannon G (2015) Femtosecond Laser Processing of Metal and Plastics. *Medical Design Technology*. Retrieved from <https://www.mdmtmag.com/article/2015/08/femtosecond-laser-processing-metal-and-plastics>
- Kirkwood SE, Tsui YY, Fedosejevs R, Brantov AV and Bychenkov VY (2009) Experimental and theoretical study of absorption of femtosecond laser pulses in interaction with solid copper targets. *Physical Review B* **79**(14), 144120.
- Lewis LJ and Perez D (2009) Laser ablation with short and ultrashort laser pulses: basic mechanisms from molecular-dynamics simulations. *Applied Surface Science* **255**(10), 5101–5106.
- Li Q, Lao H, Lin J, Chen Y and Chen X (2011) Study of femtosecond ablation on aluminum film with 3D two-temperature model and experimental verifications. *Applied Physics A* **105**(1), 125–129.
- Lin Z (2007) Temperature dependences of the electron–phonon coupling, electron heat capacity and thermal conductivity in Ni under femtosecond laser irradiation. *Applied Surface Science* **253**(15), 6295–6300.
- Lin Z, Zhigilei LV and Celli V (2008) Electron-phonon coupling and electron heat capacity of metals under conditions of strong electron-phonon non-equilibrium. *Physical Review B* **77**(7), 75133.

- Loboda PA, Smirnov NA, Shadrin AA and Karlykhanov NG** (2011) Simulation of absorption of femtosecond laser pulses in solid-density copper. *High Energy Density Physics* 7(4), 361–370.
- Mannion P, Magee J, Coyne E, O'Connor G and Glynn T** (2004) The effect of damage accumulation behaviour on ablation thresholds and damage morphology in ultrafast laser micro-machining of common metals in air. *Applied Surface Science* 233(1–4), 275–287.
- Miotello A and Kelly R** (1995) Critical assessment of thermal models for laser sputtering at high fluences. *Applied Physics Letters* 67(24), 3535.
- Perez D and Lewis LJ** (2002) Ablation of Solids under Femtosecond Laser Pulses. *Physical Review Letters* 89(25), 255504.
- Perez D and Lewis LJ** (2003) Molecular-dynamics study of ablation of solids under femtosecond laser pulses. *Physical Review B* 67(18), 184102.
- Polek MP** (2015) *Effects of femtosecond laser irradiation of metallic and dielectric materials in the low-to-high fluence regimes*, MS thesis, Purdue University.
- Preuss S, Demchuk A and Stuke M** (1995) Sub-picosecond UV laser ablation of metals. *Applied Physics A Materials Science & Processing* 61(1), 33–37.
- Price DF, More RM, Walling RS, Guethlein G, Shepherd RL, Stewart RE and White WE** (1995) Absorption of ultrashort laser pulses by solid targets heated rapidly to temperatures 1–1000 eV. *Physical Review Letters* 75(2), 252–255.
- Schmidt V, Husinsky W and Betz G** (2002) Ultrashort laser ablation of metals: pump–probe experiments, the role of ballistic electrons and the two-temperature model. *Applied Surface Science* 197, 145–155.
- Sokolowski-Tinten K, Bialkowski J, Cavalleri A, Von der Linde D, Oparin A, Meyer-ter-Vehn J and Anisimov SI** (1998) Transient states of matter during short pulse laser ablation. *Physical Review Letters* 81(1), 224–227.
- Suslova A and Hassanein A** (2017a) Femtosecond laser absorption, heat propagation, and damage threshold analysis for Au coating on metallic substrates. *Applied Surface Science* 422, 295–303.
- Suslova A and Hassanein A** (2017b) Simulation of femtosecond laser absorption by metallic targets and their thermal evolution. *Laser and Particle Beams* 35(3), 415–428.
- Suslova A and Hassanein A** (2018) Numerical simulation of ballistic electron dynamics and heat transport in metallic targets exposed to ultrashort laser pulse. *Journal of Applied Physics* (under review).
- Wang SY, Ren Y, Cheng CW, Chen JK and Tzou DY** (2013) Micromachining of copper by femtosecond laser pulses. *Applied Surface Science* 265, 302–308.
- Wellershoff S-S, Hohlfeld J, Gdde J and Matthias E** (1999) The role of electron–phonon coupling in femtosecond laser damage of metals. *Applied Physics A* 69, 99–107.
- Yang J, Zhao Y and Zhu X** (2007) Theoretical studies of ultrafast ablation of metal targets dominated by phase explosion. *Applied Physics A* 89(2), 571–578.
- Zhao X** (2014) *Ultrashort Laser Pulse - Matter Interaction: Fundamentals and Early Stage Plasma Dynamics*. PhD thesis, Purdue University, IN.
- Zhigilei LV, Ivanov DS, Leveugle E, Sadigh B and Bringa EM** (2004) Computer modeling of laser melting and spallation of metal targets. In C. R. Phipps, ed., *High-Power laser Ablation V*, SPIE Proceedings, p. 15.
- Zhigilei LV, Lin Z and Ivanov DS** (2009) Atomistic modeling of short pulse laser ablation of metals: connections between melting, spallation, and phase explosion. *The Journal of Physical Chemistry C* 113(27), 11892–11906.